Research Article | Vol. 28, No. 17 / 17 August 2020 / Optics Express 24599

Optics EXPRESS

Dynamics of the femtosecond laser-triggered spark gap

E. W. ROSENTHAL,[1] I. LARKIN,[1] A. GOFFIN,[1] T. PRODUIT,[2] M. C. SCHROEDER,[2] J.-P. WOLF,[2] AND H. M. MILCHBERG[1,*]

[1] *Institute for Research in Electronics and Applied Physics, University of Maryland, College Park, MD 20742, USA*

[2] *Dept. of Applied Physics, University of Geneva, Chemin de Pinchat 22, 1211 Geneva 4, Switzerland*

[*] *milch@umd.edu*

Abstract: We present space and time resolved measurements of the air hydrodynamics induced by femtosecond laser pulse excitation of the air gap between two electrodes at high potential difference. We explore both plasma-based and plasma-free gap excitation. The former uses the plasma left in the wake of femtosecond filamentation, while the latter exploits air heating by multiple-pulse resonant excitation of quantum molecular wavepackets. We find that the cumulative *electrode-driven* air density depression channel plays the dominant role in the gap evolution leading to breakdown. Femtosecond laser heating serves mainly to initiate the depression channel; the presence of filament plasma only augments the early heating.

1. Introduction

Considerable work has been done over the past several decades investigating the triggering of high voltage (HV) gas discharges by intense laser pulses. Spark gap discharges are used in widespread applications including HV surge protection and power switching, high energy laser triggering, and as ignition sources in combustion engines. The theory of spark-gap discharges is rich in basic physics and has been discussed at length in the literature [1–10]. Spark gaps rely on acceleration of free electrons between the cathode and anode by the gap electric field, driving further ionization by collisional avalanche ionization. In the conventional picture, breakdown starts with the development of one or more 'streamers', i.e. avalanche-ionization induced protrusions of charge, which under the action of additional resistive heating of the gas and consequent lowering of neutral gas density, create a higher conductance channel bridging the cathode and anode. Laser heating of the intra-gap gas can enable control of the discharge current path [11]. The use of low energy ultrafast laser pulses can improve this control by generating, via multiphoton or field ionization, a continuous extended length of low density plasma [12]. Extended focal volumes can be generated by optical elements such as cylindrical lenses or axicons [12] or by relying on nonlinear self-guiding by femtosecond filamentation [13,14]. In the case of filamentation in air, on-axis electron densities are typically $\lesssim 10^{16}$ cm^{-3} [15], constituting only ~0.1% fractional ionization at atmospheric density. Few-nanosecond Q-switched lasers, by contrast, can generate higher plasma densities through electron avalanche, but longitudinally extended and contiguous energy deposition is a challenge. The use of double pulse schemes [12,16] or picosecond lasers [17] have been proposed as solutions providing higher density contiguous plasmas.

Regardless of the pulsewidth used, laser triggering of HV discharges in past work has depended on gas ionization by the laser, with the discharge initiated either by the newly conductive channel enabled by the plasma [18], or by the reduced gas density channel driven hydrodynamically by the gas heating [19–21], where in the latter case the lower density reduces the breakdown threshold electric field [22]. For femtosecond pulses, because of the relatively low plasma densities and conductivity generated, it has been proposed that hydrodynamic response and on-axis density reduction is the primary mechanism responsible for discharge initiation [20,21].

#398836 https://doi.org/10.1364/OE.398836
Journal © 2020 Received 28 May 2020; revised 13 Jul 2020; accepted 20 Jul 2020; published 5 Aug 2020

Optics EXPRESS

Femtosecond filament triggered HV discharges have been widely studied in recent years, with applications envisioned to include reconfigurable RF antennas and guiding of electrical pulsed power, including lightning [23–28].

Early work by Loeb [6–8] and Meek [9] explained HV breakdown discharges in terms of streamer formation. The role of streamers and the associated phenomena of leaders and corona discharge have generated much discussion in the femtosecond laser discharge literature on both long and short spark gaps in air. Several groups have determined that corona generation and leader formation are important for filament-guided HV breakdowns in air [20,29–31]. Gordon *et al.* demonstrated a mode of discharge which can proceed without the aid of streamers, where electric field-driven resistive heating by free electrons in the gap increases the temperature and plasma lifetime, leading to breakdown [32]. Schmitt-Sody *et al.* also demonstrated streamer-free HV discharges triggered by > 2 ps duration pulses [33].

In this paper, we perform space- and time-resolved measurements of the plasma and gas evolution in a high voltage electrode gap at times after the application of an ultrashort laser pulse or pulse train up to the point of breakdown. We find that the cumulative electrode-driven air density depression channel initiated by the laser and sustained by the gap field plays the dominant role in the gas evolution leading to breakdown. Even at voltages well below breakdown, the cumulative resistive heating induced by the gap field acts to deepen and widen a reduced density air channel between the electrodes. Approaching breakdown, the air channel guides the streamers, promotes secondary ionization, and reduces the threshold voltage. We show that the size of the initial axial air density depression induced by the laser, irrespective of whether plasma is initially present or not, is what is most important for initiating a discharge. Below the breakdown threshold, we find that the transient currents induced by femtosecond laser excitation of the gap decay on a timescale consistent with transverse thermal diffusion of the reduced density channel.

2. Experimental setup

The spark gap consists of two hemispherical tungsten electrodes of radius $a_{elec} = 1.27$ cm spaced 3 mm−10 mm apart, with 2 mm diameter axial holes for entrance and exit of the heating laser pulse or pulse train, plus an interferometric probe pulse (see Fig. 1(a)). To generate pulse trains, single pulses from a Ti:Sapphire laser (λ=800 nm) were first passed through a nested interferometer [34] ('pulse stacker') which generates eight replica pulses, with the inter-pulse delays controlled by motorized translation stages (~10 fs step size). For single pulse experiments, all but one of the pulse stacker arms was blocked. The pulse or pulse train was then passed through an adjustable grating compressor allowing control of the pulsewidth. Inserting the pulse stacker upstream of the compressor avoided nonlinear distortion in the stacker's beamsplitting optics. The laser was then axially focused through the electrode holes (using a $f = 50$ cm lens at $f/45$), giving a confocal parameter of $2z_0 = 4$ mm and $1/e^2$ intensity radius $w_0 = 23$ μm, with the beam waist placed midway between the electrodes. In general, the axial extent of the gas excitation was longer than $2z_0$ owing to the onset of self-focusing and filamentation, as discussed later.

As shown in Fig. 1(a), the electrodes were connected in parallel with a C=4.4 nF capacitor bank, which was charged through a 1 kΩ resistor up to +30 kV by a DC HV power supply (Spellman High-Voltage model SL30PN10). The diode, inductor, and capacitor near the power supply act as an RF choke to shunt to ground any strong transients from the spark gap breakdown. A current measurement circuit (inside the green dashed box) is inserted in series with the spark gap ground electrode for some of our measurements. Figure 1(b) shows numerical solutions of Laplace's equation giving the on-axis electric field $E_z(z)$ between the electrodes for a range of electrode spacings and a nominal gap voltage of 10 kV. The two short vertical black lines on each curve indicate the front faces of the two hemispherical electrodes, with the electric field quickly decreasing inside the electrode central holes. For electrode gaps $\gtrsim$4 mm, $E_z(z)$ is reasonably

Optics EXPRESS

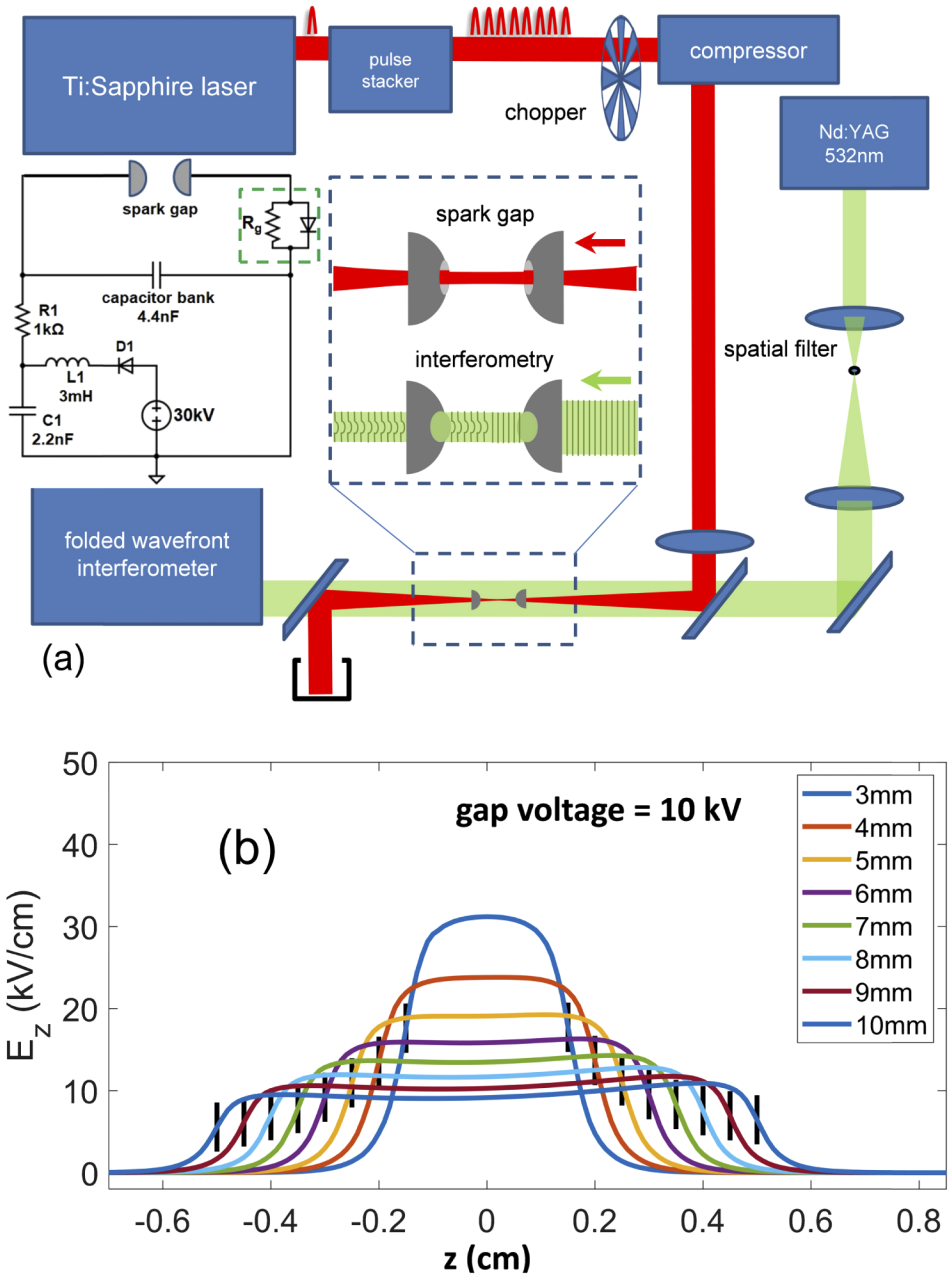

Fig. 1. **(a)** Optical setup for investigating gas density dynamics initiated by a λ=800 nm femtosecond laser pulse or pulses in a high voltage spark gap. The magnified view shows the femtosecond excitation pulse and λ=532 nm, 10 ns probe pulse propagating axially through the spark gap electrodes. Arrows depict the direction of propagation. Also shown is the spark generation circuit, with the green box depicting an auxiliary current monitor. **(b)** Simulated on-axis axial field E_z for a range of electrode separations for 10 kV gap voltage. Fields for different gap voltages are obtained by linear scaling. The two vertical black bars on each curve indicate the front faces of the hemispherical electrodes.

Optics EXPRESS

uniform between the electrodes. The gas and plasma evolution between the electrodes was monitored by a variably delayed interferometric probe pulse (λ=532 nm, 10 ns) electronically synchronized (~1 ns jitter) and co-propagating with the femtosecond air excitation pulse(s) (see Fig. 1(a)). The probe pulsewidth and timing jitter were small compared to the onset timescale of breakdown (see below).

The interaction region was end-imaged through the hole in the positive electrode onto a folded wavefront interferometer, with the object plane adjustable. Interferometric background images (femtosecond pulse off) were taken on every shot by passing the pulse(s) through an optical chopper before the compressor. The probe beam was cleaned by a spatial filter prior to the interaction region, producing smooth, low noise phase fronts. With use of the chopper, our single shot interferometric measurements were limited to a noise floor of < 40 mrad. Extraction of interferometric phase $\Delta\varphi(\mathbf{r}_\perp)$ was performed as in Ref. [35], yielding refractive index perturbation profiles $\Delta n(\mathbf{r}_\perp)$ axially averaged over the gap width, where $\mathbf{r}_\perp$ is a transverse coordinate with respect to the spark gap axis.

3. Results and discussion

Figure 2 shows a time sequence of air density perturbation profiles $\Delta N(\mathbf{r}_\perp)/N_0 = \Delta n(\mathbf{r}_\perp)/(n_0 - 1)$ following application of a 65 μJ, 100 fs FWHM laser pulse to a 5.5 mm electrode gap for (a) 0 V and (b) 17 kV/cm applied to the gap. Here N_0 and n_0 are the background air density and refractive index, respectively. Based on measurements and simulations in our prior work [35–37], the profiles in (a) are explained as follows. When a 50-100 fs laser pulse is focused into air, energy is deposited primarily through optical field ionization and non-resonant rotational Raman excitation of the air molecules (the laser bandwidth is not wide enough for vibrational Raman excitation) [38].

The laser-produced plasma recombines to neutral gas on a <10 ns timescale [15,39], while the excited molecular rotational wavepacket collisionally decoheres on a ~100 ps timescale [38]. Owing to the finite thermal conductivity of the surrounding air, the deposited laser energy remains contained in a narrow radial zone, but is repartitioned into the translational and rotational degrees of freedom of the neutral gas [35]. For femtosecond filamentation in atmosphere, the radial zone has approximately the filament core radius of $a_{core} \sim 50\ \mu$m [15,35, 40]. The result is an extended region of high pressure at temperatures up to a few hundred K above ambient [36]. The onset of this pressure spike is much faster than the acoustic timescale of the gas, $a_{core}/c_s \sim 100$ ns, where $c_s \sim 3.4 \times 10^4$ cm/s is the air sound speed, so that it impulsively launches a cylindrical single-cycle acoustic wave ~100 ns after the filament is formed [37], as seen in Fig. 2(a). Later panels show that by ~1 μs, the acoustic wave has long since left the filament region, leaving a density depression ('density hole') at elevated temperature and in pressure equilibrium with the surrounding gas. Over $> \sim 1\ \mu$s to ~1 ms, the density hole decays by thermal diffusion, becoming shallower and wider.

After pressure equilibrium has been achieved, the 'area' of the density hole profile is a proxy for the laser energy deposited per unit length in the gas, as shown in Ref. [41],

$$\varepsilon_{abs} = -(k(n-1))^{-1} c_v T_0 \rho_0 \int \Delta\varphi(\mathbf{r}_\perp) d^2\mathbf{r}_\perp, \tag{1}$$

where c_v is the specific heat of air at constant volume, ρ_0 and T_0 are the ambient gas density and temperature, $k = 2\pi/\lambda$ is the probe wavenumber, and n is the gas refractive index. While Eq. (1) was applied in Ref. [41] to femtosecond laser-generated density holes, it will also apply to calculating energy deposited by any heating mechanism that is fast compared to thermal diffusion into the surrounding gas, which has a ~millisecond timescale. We use this broader applicability of Eq. (1) in much of the analysis of this paper.

Optics EXPRESS

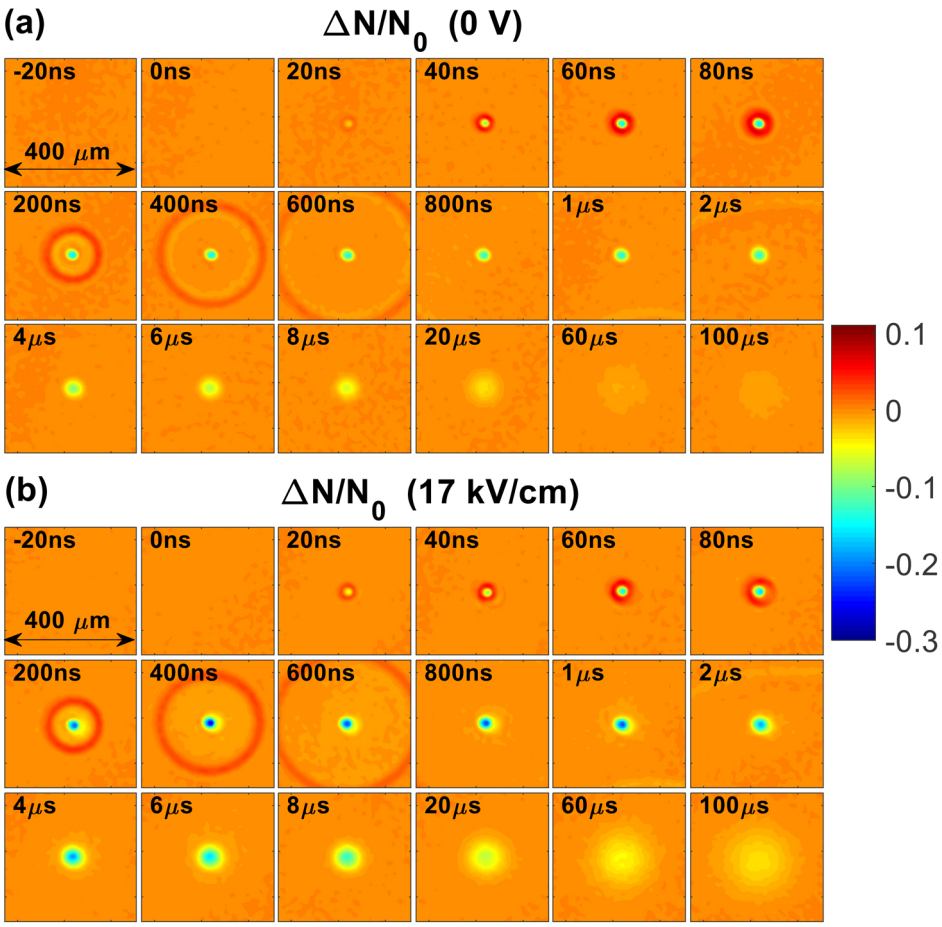

Fig. 2. **(a)** Evolution of relative air density shift at a sequence of probe delays following heating at $t = 0$ by a single 100 fs, 65 μJ laser pulse in the spark gap with zero gap field. The outward propagating orange ring, seen in the frames at delays < 800 ns, is a single-cycle acoustic wave. **(b)** Same measurement as (a), but with 17 kV/cm gap field. In the case of HV applied across the gap, the on-axis density hole is observed to deepen and widen relative to the 0 V case at all delays, and acoustic wave amplitude is larger. Gap length=5.5 mm.

3.1. Role of filament plasma and density hole in high voltage breakdown

We first assess the roles of the laser produced plasma and the gas density depression in the high voltage breakdown process. A first set of experiments was performed in which air density holes of the same depth were generated, either with or without initial plasma. In the case of a single filamenting pulse that generates plasma in the usual manner, the pulse energy was chosen (22 μJ, 100 fs) to produce an on-axis density hole depth $\Delta N/N_0 \sim 3\%$ at 1 μs delay after the pulse, where N_0 is the background air density and ΔN is the on-axis density reduction. In the plasma-free case, we achieved the same $\Delta N/N_0 \sim 3\%$ hole depth at 1 μs delay by using an 8-pulse sequence of 12.5 μJ, 100 fs pulses (below the ionization threshold of the oxygen molecule) from the pulse stacker to rotationally heat the air's nitrogen molecules. The inter-pulse timing in the sequence was adjusted to ~ 8.3 ps (the rotational revival time of N_2) in order to maximize the rotational wavepacket excitation and air heating [42]. On the basis of oxygen's ionization rate intensity

Optics EXPRESS

dependence, $\propto I^8$, we expect single pulse excitation to produce at least (22 μJ/12.5 μJ)^8 ~ 90× more plasma than the pulse sequence.

Figure 3(a) shows, for the plasma and near plasma-free cases, the energy deposited in the gas between the electrodes (calculated using Eq. (1) from the gas density hole measured at 1 µs probe delay) as a function of applied gap field. The gap field used here and in all other figures is the average electric field E_z between the electrodes calculated from Fig. 1(b). Each point is an average over 25 consecutive laser shots, while the error bars correspond to the standard deviation. The plotted points terminate where breakdown occurs. Below ~13 kV/cm, the energy absorbed in the gas (~0.05 µJ) in both cases is consistent with the $\Delta N/N_0$ ~ 3% density hole imprinted by the single pulse or pulse train. Above ~13 kV/cm, there is increasing gas heating in the single pulse (plasma) case, consistent with electron impact ionization and resistive heating driven by the high voltage. At the ~13 kV/cm threshold, $eE_{gap}\lambda_{mfp}$ ~ 1 eV for a mean free path in air λ_{mfp} ~ 0.5 μm [43,44]. This is sufficient for electrons to reach several eV over multiple collisions or in the tail of the distribution, enough energy to surmount the nitrogen vibrational $^2\Pi_g$ shape resonance peaking past ~2 eV [43]. We speculate that because of this vibrational energy sink, gap fields below ~13 kV/cm are unable to accelerate electrons sufficiently to accumulate the ~12-15 eV needed for impact ionization of O_2 and N_2.

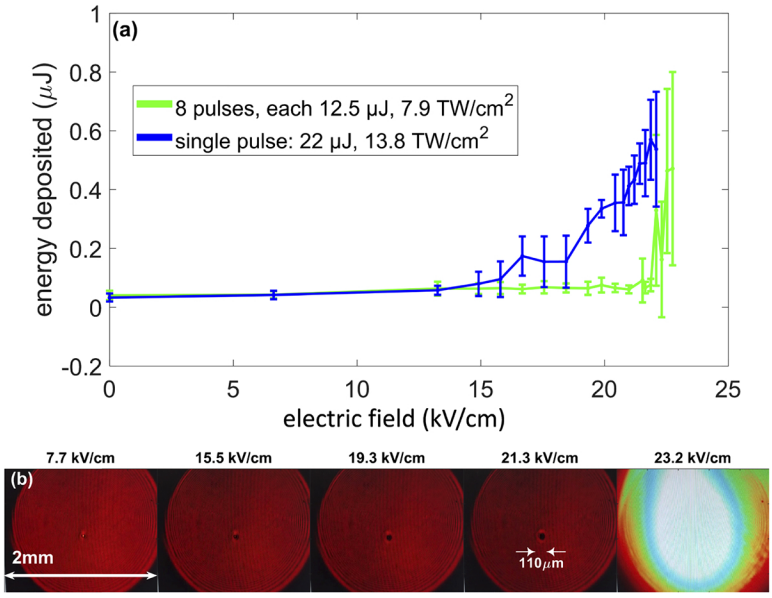

Fig. 3. **(a)** Energy deposited in the intra-gap air as a function of gap field for the case of an initial plasma (blue curve, single 22 µJ laser pulse) and the case of negligible plasma (green curve, 8 pulse sequence with 12.5 µJ/pulse). The electrode spacing is 4 mm. For the blue curve, a single laser pulse formed a plasma filament between the electrodes. For the green curve, the air in the electrode gap was heated via N_2 rotational excitation by the resonant 8-pulse sequence. In both cases, the initial on-axis density hole depth was $\Delta N/N_0$ ~ 3% at a delay of 1 µs. **(b)** End-view shadowgrams (through positive electrode) of the gas density hole initiated by single 22 µJ pulse and subsequently deepened/widened by increasing gap fields. The circular edge in the red images is the electrode central hole edge. Probe delay = 3 µs. The 23.2 kV/cm frame shows an end view of the breakdown flash. The breakdown is centered on the density hole.

Both the additional carriers and the higher energy electrons then heat the air via elastic and inelastic collisions, rapidly deepening the density hole and increasing λ_{mfp} until the onset of

Optics EXPRESS

breakdown at ~22 kV/cm, as seen in the blue curve. In both plasma-free and plasma cases, however, the breakdown threshold is ~22-23 kV/cm, and occurs roughly where the energy absorbed by the gas (as measured by the density hole area (or volume = area × length)) is comparable at ~0.5μJ. This suggests that the density hole is the main factor in setting the breakdown threshold. To the extent that pre-existing free electrons are involved, their acceleration in the gap field serves mainly to heat the air to augment the density hole. In the nominally plasma-free case (green curve), pre-breakdown gas heating has occurred, but mainly at fields just below the breakdown level. In another view of the dynamics induced by a single pulse, Fig. 3(b) shows the deepening and widening of the density hole with increasing gap field, until breakdown, centered on the density hole, occurs at ~23 kV/cm.

In the next set of experiments, we examined the effect of the energy of a single filamenting (plasma-producing) laser pulse on the onset of breakdown. Figure 4 plots energy deposition, determined via Eq. (1), as a function of gap field (gap length 5.5 mm) for four laser pulse energies. It is seen that for higher pulse energy, more energy is deposited in the gap and the gap breakdown field (where the curves terminate) is reduced. At fields below the sharp upturn of each curve, the energy deposition is seen to slowly increase or stay roughly constant. For each curve, the upturn is associated, as in Fig. 3, with the onset of sufficient electron acceleration for impact ionization of O_2 and N_2 along with increasing gas heating and widening/deepening of the density hole, which increases channel conductivity. The higher initial electron densities generated by higher laser energies establish larger density hole volumes, leading to onset of breakdown at lower gap fields.

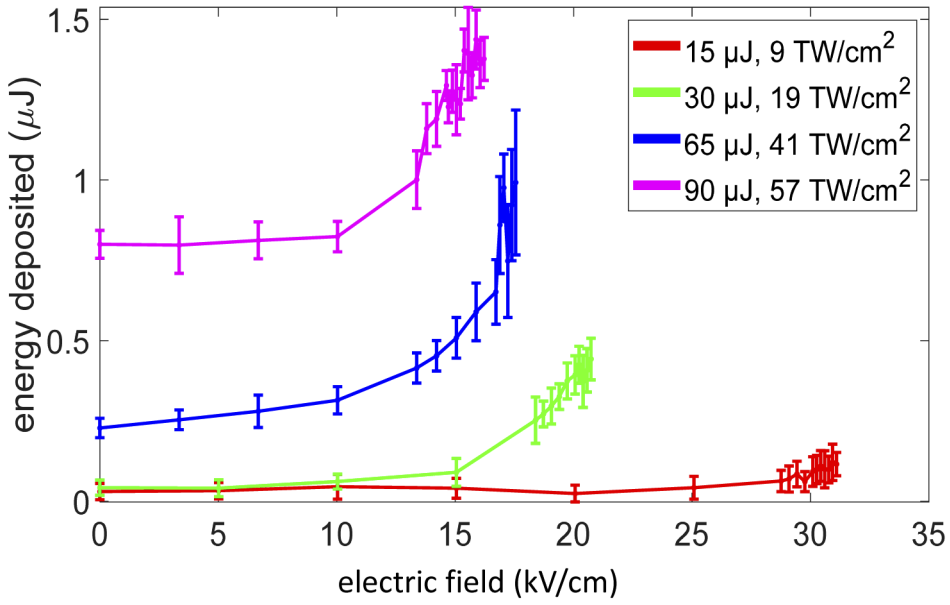

Fig. 4. Energy deposited in the intra-gap air as a function of the input laser pulse energy and gap field for a 5.5 mm gap. The curves terminate at the point of breakdown.

3.2. *Effect of spark gap electrode separation*

Figure 5(a) demonstrates the dependence of air heating in the gap (by a single 75 μJ pulse) as a function of gap electric field for a range of electrode separations (4mm - 10mm). Each curve in Fig. 5(a) terminates at the breakdown field near ~15 kV/cm. For the smaller gaps, the effective breakdown field is slightly larger (~16 kV/cm) because, as seen in Fig. 1(b), the field peaks over

Optics EXPRESS

a smaller fraction of the gap width. For the longer gaps, the peak field occupies a larger fraction of the gap; the breakdown field converges to ~14-15 kV/cm.

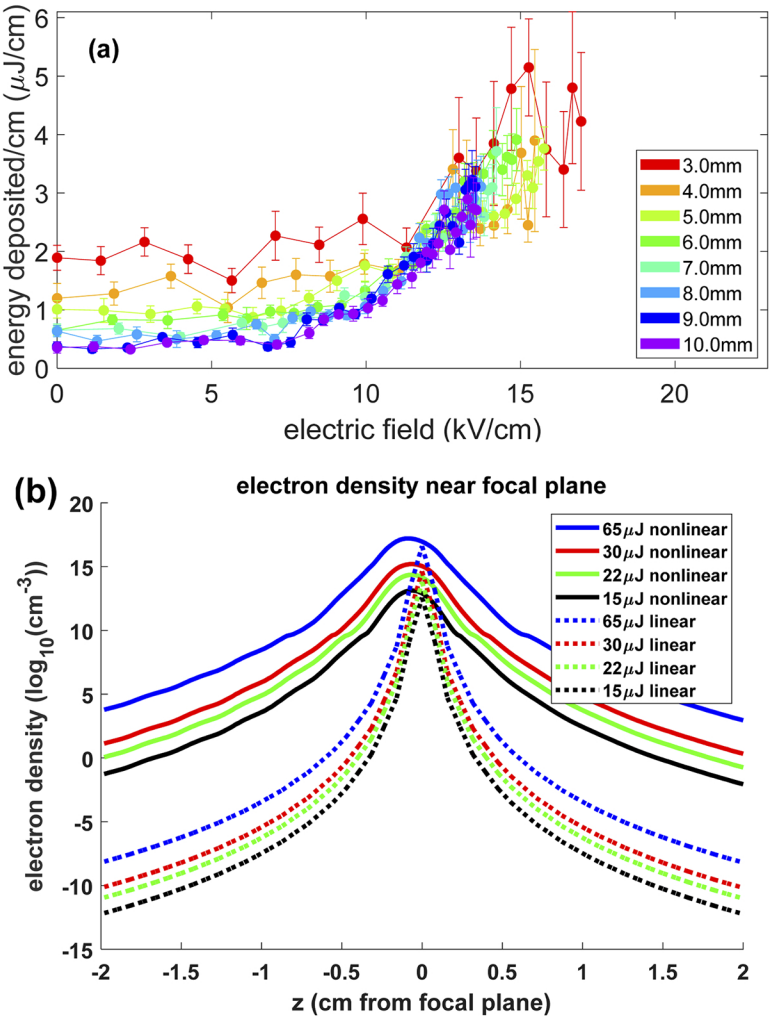

Fig. 5. **(a)** Energy deposited per unit length after single 75 μJ laser pulse excitation for a range of gap fields and gap separations. **(b)** Propagation simulation showing the plasma-extending effect of filamentation. The laser propagates left to right. By comparison, the multiphoton ionization yield of a linearly propagating pulse is many orders of magnitude lower away from the linear beam waist. It is seen that filament peak electron density occurs slightly upstream of the linear beam waist consistent with self-focusing and filamentation.

In all of these runs, the laser vacuum confocal parameter is $2z_0 \sim 4$ mm centred on the gap, with spot size $w_0 = 23\ \mu m$. However, filamentary propagation is responsible for extended plasma generation, increasing the electron density away from the vacuum beam waist by many orders of magnitude. This is seen in the filamentation simulations of Fig. 5(b), which are compared to the $\propto(I(z))^8$ ionization yield of a linearly propagating pulse. These simulations were performed with a GPU implementation of the unidirectional pulse propagation equation, which includes the full molecular response of air [45,46]. The plots of Fig. 5(a) show that for low fields, the energy deposition per unit length remains roughly constant, and is higher for smaller gaps. This is consistent with laser energy deposition from the filament plasma, whose axial average electron

Optics EXPRESS

density is higher for short gaps (see Fig. 5(b)). Only once the field increases to ~8 kV/cm, the curves for all gaps begin to converge as resistive heating (by electrons driven by the gap field) begins to dominate.

3.3. Time dependence of intra-gap gas heating

Without applied HV, after the filament-heated air sheds its single cycle acoustic emission and achieves pressure equilibrium (as seen in Fig. 2(a) for $t > \sim 200$ ns), the density hole decreases in depth and widens as thermal diffusion occurs to the surrounding air. With the application of HV across the gap, the gas is heated for at least ~100μs (see below) after the initial filament energy deposition (as seen by the HV-driven widening and deepening of the density hole in Fig. 2(b)). Figure 6 shows plots of the gas heating as a function of time in a 5.5mm gap for a range of voltages for a fixed filamenting laser pulse (65 μJ, 100 fs). The highest voltage was intentionally kept just below the breakdown threshold. By t = 200 ns (indicated by the vertical black line), the acoustic wave has just been shed from the density hole. It is only after that time that Eq. (1) can be used to determine absorbed energy. It is seen that by ~200ns, the gap HV has already heated the air, as indicated by the increasing density hole volume with gap voltage, and heating is shown increasing out to at least ~100 μs. This heating remains predominantly localized to the density hole region imprinted by the initial laser pulse, as seen in Fig. 2(b) and Fig. 3(b).

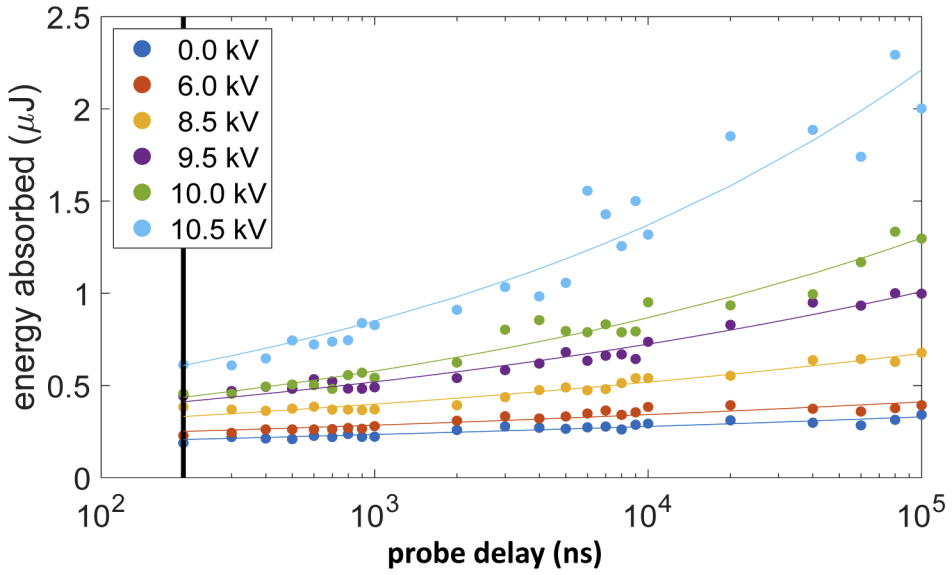

Fig. 6. Energy absorbed by intra-gap air vs. probe delay for several gap voltages. Single 65 μJ, 100 fs laser pulse, 5.5 mm gap. The vertical bar corresponds to t = 200 ns probe delay, after which Eq. (1) can be applied. The density hole volume (=area × length) is seen to continuously increase out to the maximum probe delay of 100 μs, with an increasingly rapid increase with gap voltage. Each point is an average of 25 shots, and the curves are best fits of the points to $y = at^b$. Even by 200ns, higher gap voltages drive significant heating.

3.4. Pre-breakdown gap current measurements

To help understand the origin of the pre-breakdown air heating, we inserted an auxiliary current monitor shown by the dashed green box in Fig. 1(a). It consists of a resistance R_g = 9.1 MΩ in parallel with a miniature gas discharge tube (LittelFuse CG110) linked to ground from the gap electrode. The discharge tube acts as a shunt to ground for the extremely large transient

Optics EXPRESS

currents generated at spark gap breakdown. A high voltage probe (Tektronix P6139B) measures the time-resolved voltage $V_R(t)$ and gap current $I_{gap}(t) = V_R(t)/R_g$ for gap voltage below the breakdown threshold, where R_g includes the contribution of the voltage probe resistance.

Results are shown in Fig. 7(a) for both the single 22 μJ, 100 fs filamenting laser pulse (blue curves) and the 8-pulse (12.5 μJ, 100fs) resonant sequence (green curves) in a 4 mm gap for gap fields below breakdown. Recall that the single pulse and pulse sequence generate a similar initial air density depression, but the single pulse generates plasma while there is negligible plasma from the pulse sequence. In both cases, the gap current exhibits a sharp rise at $t = 0$ immediately after application of the laser pulse, followed by a rollover and then a decay, which is well-fitted by exponentials (dashed red lines) with $\tau_{1/e} = 110 \pm 10$ μs applying to all curves. The measured sharp rise onset of ~10 ns is limited by the probe and oscilloscope frequency response. As the gap field increases, the rollover part of the curves shorten. For lower gap fields we see that the rollover duration is $< \sim 0.25$ ms, much longer than the <10 ns timescale for filament plasma recombination. This, plus the fact that the blue curves (initial plasma present) and green curves (negligible initial plasma) are similar, suggests that the driven currents are electrode-supplied; the filament-generated free electrons play a negligible direct role in the blue curves—their main, indirect, role is to initially heat the air to generate a density depression channel. This is also seen in the absorbed energy measurements at early times in Fig. 6.

We attribute the fast initial rise of the current in Fig. 7(a) to rapid streamer onset and preferential channeling through the initial axial density depression. The heating effect from preferential channeling of gap current is directly seen by comparing Fig. 2(b) to Fig. 2(a). The slow initial current increase during the rollover accompanies increasing resistive heating and channel deepening. When transverse thermal diffusion has widened the channel sufficiently, as seen in Fig. 2, the local current density drops and resistive heating decreases—the accompanying increase in gap resistance leads to a slow decrease in the current as the air gap returns to equilibrium.

For increasing gap fields, the peak of the current rollover moves to earlier times, as seen in Fig. 7(a) and in more detail in Fig. 8(a), for the 8-pulse (no initial plasma) sequence. At the highest fields, the rollover peak moves toward ~5 μs, a range consistent with the few microsecond delays for the deepest channels in Fig. 2(b). This is consistent with our observation that as the gap field increases, the deepest channels occur at earlier times.

A rough estimate of the current decay timescale after the rollover is simply the time for thermal diffusion to double the radius of the initial laser-induced channel, $\tau_{decay} \sim R^2/4\alpha$ [35], where $\alpha = 0.19$ cm^2/s is the thermal diffusivity of room temperature air [47] and we use $R = 100$ μm as twice the initial channel radius. This gives $\tau_{decay} \sim 130\mu$s, of the same scale as in Fig. 7(a).

Figure 7(b) plots the total charge $Q_{gap} = \int I_{gap}(t)dt$ as a function of gap voltage for the single pulse (plasma) and 8-pulse (plasma-free) gap excitations of Fig. 7(a), with the curves terminating at breakdown. Here it clear that the pre-breakdown charge driven across the gap increases with gap field, largely owing to electrode-supplied carriers traversing the increasingly conductive air channel. While the charge driven in the initial plasma-free laser excitation case (green curve) is somewhat lower than the initial plasma case (blue curve), the curves converge near breakdown. Measurements of Q_{gap} enable an extreme upper estimate of average electron density $\overline{N_e}$ in the gap during the current pulse: $Q_{gap} \sim \overline{N_e}\pi a^2 L_{gap}$, where $a \sim 50$ μm is the approximate air channel radius (see Fig. 2(b)) and $L_{gap} = 4$ mm is the gap spacing. Using the plot maximum $Q_{gap} \sim 20$ pC gives $\overline{N_e} \sim 4 \times 10^{12}$ cm^{-3}. This is orders of magnitude lower than the electron density generated in our femtosecond filaments (see Fig. 5(b)), further supporting the picture that electrons from the filament plasma contribute little *directly* to these current pulses.

Figure 8(b) shows the peak current using the two sets of laser parameters of Fig. 3 and Fig. 7 giving initial plasma (blue curve) and negligible initial plasma (green curve). As discussed earlier, the pulse energies were chosen so that the initial density depression was $\Delta N/N_0 \sim 3\%$ for each case. A laser-free curve (red) is plotted for comparison, where below breakdown, the current

Optics EXPRESS

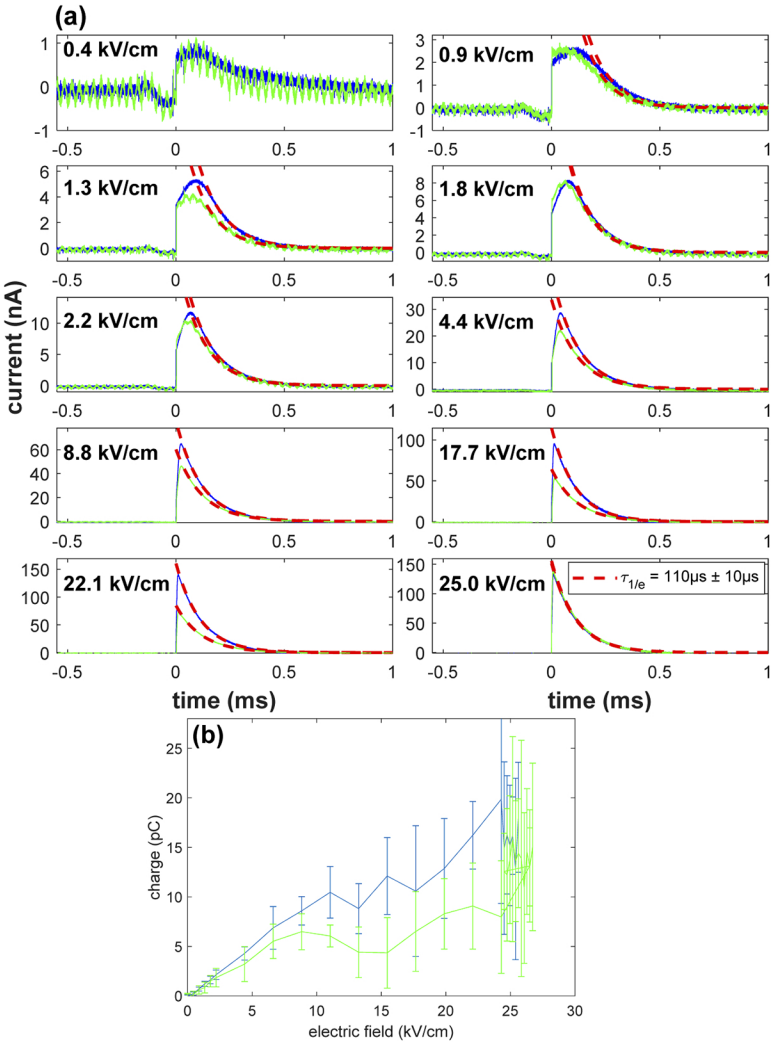

Fig. 7. (**a**) Transient gap current initiated by single 22μJ, 100 fs laser pulse (blue curves, initial plasma present) or 8-pulse 12.5 μJ, 100fs sequence (green curves, negligible initial plasma) as a function of gap field in a 4mm gap. Dashed red lines are exponential fits to the curve decay portions; all fits have $\tau_{1/e} = 110 \pm 10\ \mu s$, as indicated in bottom right panel. Curves are 10 shot averages. **(b)** Pre-breakdown charge driven across gap vs. gap field. The curves terminate at breakdown.

Optics EXPRESS

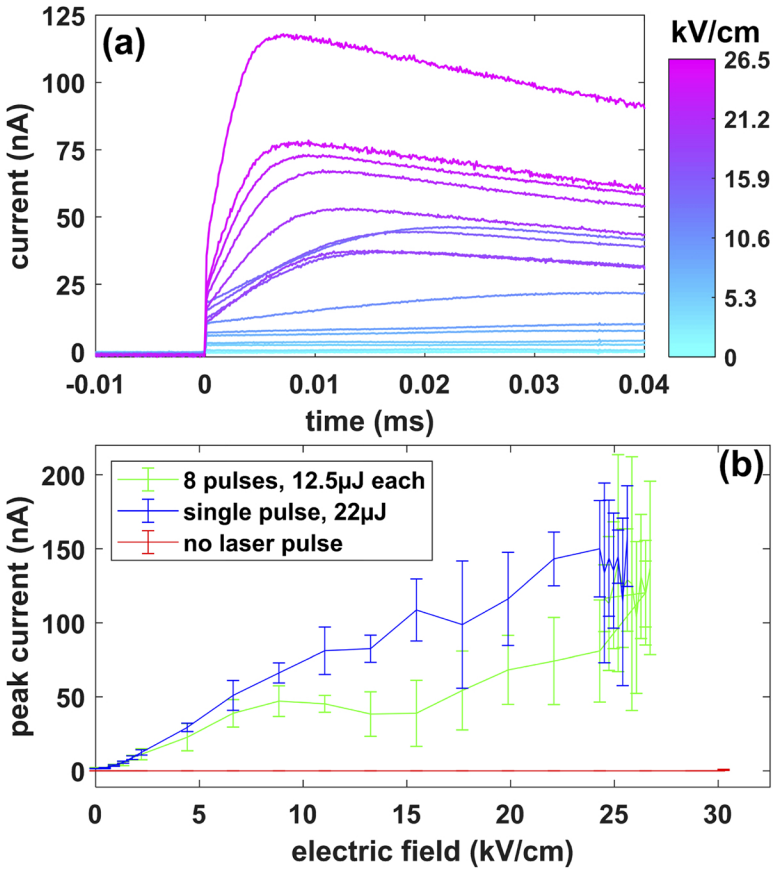

Fig. 8. Current measurements (below the breakdown threshold) using the green-boxed current monitor depicted in Fig. 1(a). **(a)** Transient gap current vs gap field induced by the 8-pulse (12.5μJ, 100 fs, no plasma) sequence. **(b)** Peak gap current vs. gap field below the breakdown threshold for the single pulse (blue, plasma) and 8-pulse (green, no plasma) cases. The blue and green curves converge and terminate where breakdown occurs at ~25 kV/cm. The no-laser case (red) is shown for comparison; breakdown occurs near ~30 kV/cm.

is zero. As in the case for total charge (Fig. 7(b)), the peak current for the single pulse case increases vs. gap field more than in the 8-pulse case, owing to its higher initial electron density and increased electrode-driven air heating and channel depth (as seen in Fig. 6). Even though the 8-pulse train generates less than ~1% of the electron density of the single pulse (see earlier discussion), the peak current is roughly 50% of the single pulse case until they converge when the gap voltage is close to the breakdown threshold. This again strongly suggests that the main role of the laser—whether through generating filament plasma or by rotational excitation—is to initially heat the air and increase the density hole or channel depth to provide enhanced channel conductance; thereafter, free carriers are largely supplied by the gap electrode. In both cases, at sufficiently high gap voltage, the carriers increase in number owing to impact ionization and continue to resistively heat the gas, increasing the density hole volume and conductance. Just before breakdown, the currents are comparable (Fig. 8(b)) as are the density hole volumes (Fig. 3).

Optics EXPRESS

4. Summary

We have measured the spatial and temporal dynamics of air heating in an ultrashort laser-triggered spark gap prior to breakdown. We find that once a reduced density air channel is created between the electrodes, regardless of how it was formed, it acts as a preferred channel through which subsequent gap field-driven current may flow. This current resistively heats the channel further, deepening it and increasing conductance and current, leading to eventual breakdown for sufficient gap field. Below the breakdown threshold field, laser-triggered current transients in the gap decay as the air depression channel becomes shallower and wider from transverse thermal diffusion.

To elucidate the relative roles of the plasma and the air density depression channel (density hole) induced by the laser, we performed gap current measurements and longitudinal interferometry through the gap electrodes. In the case of plasma and density hole generation by a single filamenting pulse, the electrons are initially driven by the gap field and further heat the air and deepen the depression channel, with subsequent current provided by the electrodes and channeled through the density hole. In the case of little plasma but comparable density hole generation from an 8-pulse sequence, the lower current initially provided by the electrodes is preferentially channeled through the density hole, heating it further. As gap voltage is increased, impact ionization increases the gap current to the point where the current and the density hole volume in both cases are comparable. This leads to similar breakdown thresholds. Below the breakdown threshold, laser excitation of the gap triggers an electrode-supplied current transient through the reduced density channel. As the channel widens and decreases in depth due to transverse thermal diffusion, the current decays on the thermal diffusion time scale of ~100 μs and the air gap returns to a non-conducting equilibrium.

For ease of diagnostic access, we examined relatively short spark gaps; however, we expect the scenario we described here to apply to longer femtosecond filament-triggered discharges; its range of applicability will be the subject of future experiments.

Funding

Army Research Office (W911NF-14-1-0372); Air Force Office of Scientific Research (FA9550-16-1-0121, FA9550-16-1-0284); Office of Naval Research (N00014-17-1-2705, N00014-17-1-2778); Schweizerischer Nationalfonds zur Förderung der Wissenschaftlichen Forschung (200021-178926); Horizon 2020 Framework Programme (737033-LLR).

Disclosures

The authors declare no conflicts of interest.

References

1. A. H. Guenther and J. R. Bettis, "A review of laser-triggered switching," Proc. IEEE **59**(4), 689–697 (1971).
2. W. K. Pendleton and A. H. Guenther, "Investigation of a Laser Triggered Spark Gap," Rev. Sci. Instrum. **36**(11), 1546–1550 (1965).
3. A. H. Guenther and J. R. Bettis, "Laser-triggered megavolt switching," IEEE J. Quantum Electron. **3**(11), 581–588 (1967).
4. L. L. Steinmetz, "Laser-Triggered Spark Gap," Rev. Sci. Instrum. **39**(6), 904–909 (1968).
5. M. J. Kushner, R. D. Milroy, and W. D. Kimura, "A laser-triggered spark gap model," J. Appl. Phys. **58**(8), 2988–3000 (1985).
6. L. B. Loeb and A. F. Kip, "Electrical Discharges in Air at Atmospheric Pressure The Nature of the Positive and Negative Point-to-Plane Coronas and the Mechanism of Spark Propagation," J. Appl. Phys. **10**(3), 142–160 (1939).
7. L. B. Loeb and J. M. Meek, "The Mechanism of Spark Discharge in Air at Atmospheric Pressure. I," J. Appl. Phys. **11**(6), 438–447 (1940).
8. L. B. Loeb and J. M. Meek, "The Mechanism of Spark Discharge in Air at Atmospheric Pressure. II," J. Appl. Phys. **11**(7), 459–474 (1940).
9. J. M. Meek, "A Theory of Spark Discharge," Phys. Rev. **57**(8), 722–728 (1940).
10. J. S. Townsend, "The Conductivity produced in Gases by the Motion of Negatively-charged Ions," Nature **62**(1606), 340–341 (1900).

Optics EXPRESS

11. M. Miki, Y. Aihara, and T. Shindo, "Development of long gap discharges guided by a pulsed CO_2 laser," J. Phys. D: Appl. Phys. **26**(8), 1244–1252 (1993).
12. P. Polynkin, B. Pasenhow, N. Driscoll, M. Scheller, E. M. Wright, and J. V. Moloney, "Seeded optically driven avalanche ionization in molecular and noble gases," Phys. Rev. A **86**(4), 043410 (2012).
13. A. Couairon and A. Mysyrowicz, "Femtosecond filamentation in transparent media," Phys. Rep. **441**(2-4), 47–189 (2007).
14. L. Berge, S. Skupin, R. Nuter, J. Kasparian, and J.-P. Wolf, "Ultrashort filaments of light in weakly ionized, optically transparent media," Rep. Prog. Phys. **70**(10), 1633–1713 (2007).
15. Y.-H. Chen, S. Varma, T. Antonsen, and H. Milchberg, "Direct Measurement of the Electron Density of Extended Femtosecond Laser Pulse-Induced Filaments," Phys. Rev. Lett. **105**(21), 215005 (2010).
16. P. Polynkin and J. V. Moloney, "Optical breakdown of air triggered by femtosecond laser filaments," Appl. Phys. Lett. **99**(15), 151103 (2011).
17. A. Schmitt-Sody, H. G. Kurz, L. Bergé, S. Skupin, and P. Polynkin, "Picosecond laser filamentation in air," New J. Phys. **18**(9), 093005 (2016).
18. M. Rodriguez, R. Sauerbrey, H. Wille, L. Wöste, T. Fujii, Y.-B. André, A. Mysyrowicz, L. Klingbeil, K. Rethmeier, W. Kalkner, J. Kasparian, E. Salmon, J. Yu, and J.-P. Wolf, "Triggering and guiding megavolt discharges by use of laser-induced ionized filaments," Opt. Lett. **27**(9), 772 (2002).
19. K. A. Saum and D. W. Koopman, "Discharges Guided by Laser-Induced Rarefaction Channels," Phys. Fluids **15**(11), 2077 (1972).
20. A. Schmitt-Sody, D. French, W. White, A. Lucero, W. P. Roach, and V. Hasson, "The importance of corona generation and leader formation during laser filament guided discharges in air," Appl. Phys. Lett. **106**(12), 124101 (2015).
21. S. Tzortzakis, B. Prade, M. Franco, A. Mysyrowicz, S. Hüller, and P. Mora, "Femtosecond laser-guided electric discharge in air," Phys. Rev. E **64**(5), 057401 (2001).
22. F. Paschen, "On the potential difference required for spark transfer in air, hydrogen and carbonic acid at different pressures," Ann. Phys. **273**(5), 69–96 (1889).
23. G. Point, L. Arantchouk, E. Thouin, J. Carbonnel, A. Mysyrowicz, and A. Houard, "Long-lived laser-induced arc discharges for energy channeling applications," Sci. Rep. **7**(1), 13801 (2017).
24. G. Point, L. Arantchouk, J. Carbonnel, A. Mysyrowicz, and A. Houard, "Plasma dynamics of a laser filamentation-guided spark," Phys. Plasmas **23**(9), 093505 (2016).
25. Y. Brelet, A. Houard, G. Point, B. Prade, L. Arantchouk, J. Carbonnel, Y.-B. André, M. Pellet, and A. Mysyrowicz, "Radiofrequency plasma antenna generated by femtosecond laser filaments in air," Appl. Phys. Lett. **101**(26), 264106 (2012).
26. F. Théberge, J.-F. Daigle, J.-C. Kieffer, F. Vidal, and M. Châteauneuf, "Laser-guided energetic discharges over large air gaps by electric-field enhanced plasma filaments," Sci. Rep. **7**(1), 40063 (2017).
27. X. M. Zhao, J.-C. Diels, C. Y. Wang, and J. M. Elizondo, "Femtosecond ultraviolet laser pulse induced lightning discharges in gases," IEEE J. Quantum Electron. **31**(3), 599–612 (1995).
28. J. Kasparian, R. Ackermann, Y.-B. André, G. Méchain, G. Méjean, B. Prade, P. Rohwetter, E. Salmon, K. Stelmaszczyk, J. Yu, A. Mysyrowicz, R. Sauerbrey, L. Wöste, and J.-P. Wolf, "Electric events synchronized with laser filaments in thunderclouds," Opt. Express **16**(8), 5757 (2008).
29. D. Comtois, C. Y. Chien, A. Desparois, F. Génin, G. Jarry, T. W. Johnston, J.-C. Kieffer, B. La Fontaine, F. Martin, R. Mawassi, H. Pépin, F. A. M. Rizk, F. Vidal, P. Couture, H. P. Mercure, C. Potvin, A. Bondiou-Clergerie, and I. Gallimberti, "Triggering and guiding leader discharges using a plasma channel created by an ultrashort laser pulse," Appl. Phys. Lett. **76**(7), 819–821 (2000).
30. T. Fujii, M. Miki, N. Goto, A. Zhidkov, T. Fukuchi, Y. Oishi, and K. Nemoto, "Leader effects on femtosecond-laser-filament-triggered discharges," Phys. Plasmas **15**(1), 013107 (2008).
31. K. Sugiyama, T. Fujii, M. Miki, A. Zhidkov, M. Yamaguchi, E. Hotta, and K. Nemoto, "Submicrosecond laser-filament-assisted corona bursts near a high-voltage electrode," Phys. Plasmas **17**(4), 043108 (2010).
32. D. F. Gordon, A. Ting, R. F. Hubbard, E. Briscoe, C. Manka, S. P. Slinker, A. P. Baronavski, H. D. Ladouceur, P. W. Grounds, and P. G. Girardi, "Streamerless guided electric discharges triggered by femtosecond laser filaments," Phys. Plasmas **10**(11), 4530–4538 (2003).
33. A. Schmitt-Sody, J. Elle, A. Lucero, M. Domonkos, A. Ting, and V. Hasson, "Dependence of single-shot pulse durations on near-infrared filamentation-guided breakdown in air," AIP Adv. **7**(3), 035018 (2017).
34. C. W. Siders, J. L. Siders, A. J. Taylor, S. G. Park, and A. M. Weiner, "Efficient high-energy pulse-train generation using a 2^n -pulse Michelson interferometer," Appl. Opt. **37**(22), 5302 (1998).
35. Y.-H. Cheng, J. K. Wahlstrand, N. Jhajj, and H. M. Milchberg, "The effect of long timescale gas dynamics on femtosecond filamentation," Opt. Express **21**(4), 4740 (2013).
36. N. Jhajj, E. W. Rosenthal, R. Birnbaum, J. K. Wahlstrand, and H. M. Milchberg, "Demonstration of Long-Lived High-Power Optical Waveguides in Air," Phys. Rev. X **4**(1), 011027 (2014).
37. J. K. Wahlstrand, N. Jhajj, E. W. Rosenthal, S. Zahedpour, and H. M. Milchberg, "Direct imaging of the acoustic waves generated by femtosecond filaments in air," Opt. Lett. **39**(5), 1290 (2014).
38. Y.-H. Chen, S. Varma, A. York, and H. M. Milchberg, "Single-shot, space- and time-resolved measurement of rotational wavepacket revivals in H_2, D_2, N_2, O_2, and N_2O," Opt. Express **15**(18), 11341 (2007).

Optics EXPRESS

39. S. Tzortzakis, B. Prade, M. Franco, and A. Mysyrowicz, "Time-evolution of the plasma channel at the trail of a self-guided IR femtosecond laser pulse in air," Opt. Commun. **181**(1-3), 123–127 (2000).
40. S. Tzortzakis, M. A. Franco, Y.-B. André, A. Chiron, B. Lamouroux, B. S. Prade, and A. Mysyrowicz, "Formation of a conducting channel in air by self-guided femtosecond laser pulses," Phys. Rev. E **60**(4), R3505–R3507 (1999).
41. E. W. Rosenthal, N. Jhajj, I. Larkin, S. Zahedpour, J. K. Wahlstrand, and H. M. Milchberg, "Energy deposition of single femtosecond filaments in the atmosphere," Opt. Lett. **41**(16), 3908 (2016).
42. S. Zahedpour, J. K. Wahlstrand, and H. M. Milchberg, "Quantum Control of Molecular Gas Hydrodynamics," Phys. Rev. Lett. **112**(14), 143601 (2014).
43. Y. Itikawa, "Cross Sections for Electron Collisions with Nitrogen Molecules," J. Phys. Chem. Ref. Data **35**(1), 31–53 (2006).
44. Y. Itikawa, "Cross Sections for Electron Collisions with Oxygen Molecules," J. Phys. Chem. Ref. Data **38**(1), 1–20 (2009).
45. M. Kolesik and J. V. Moloney, "Nonlinear optical pulse propagation simulation: From Maxwell's to unidirectional equations," Phys. Rev. E **70**(3), 036604 (2004).
46. D. Jang, R. M. Schwartz, D. Woodbury, J. Griff-McMahon, A. H. Younis, H. M. Milchberg, and K. Y. Kim, "Efficient terahertz and Brunel harmonic generation from air plasma via mid-infrared coherent control," Optica **6**(10), 1338 (2019).
47. Y. S. Touloukian, P. E. Liley, and S. C. Saxena, "Thermal conductivity: nonmetallic liquids and gases," New York: IFI/Plenum (1970).